Supplementary information

Gas diffusion nanocomposite layer with enhanced water and gas transport by hydrophilic-superhydrophobic columnar interface

Taesik Eom[ab], Seungcheol Shin[b], Myungjin Hong[b], Eun Sang Lee[ab] and Sang Eui Lee[ab]**

[a]KIURI Center for Hydrogen Based Next Generation Mechanical System, Inha University, 36 Gaetbeol-ro, Yeonsu-gu, Incheon 21999, South Korea

[b]Department of Mechanical Engineering, Inha University, 100 Inha-ro, Michuhol-gu, Incheon 22212, South Korea

***Corresponding author**

E-mail: tseom@inha.ac.kr (T. Eom) and selee@inha.ac.kr (S.E. Lee)

Optimization of MWCNT/PTFE ratio for nanocomposite films

MWCNT/PTFE nanocomposites films as GDL substrate were fabricated with varying ratios of MWCNT to PTFE, ranging from 1:99 to 0:100. SEM analysis of the film surface before and after sintering was made to estimate the dispersibility of MWCNTs and PTFE in the nanocomposite film. Before sintering (Supplementary Fig. 1a), the images revealed that as MWCNT content in the film increased, the presence of PTFE particles decreased. MWCNTs were observed to be uniformly dispersed throughout the film, appearing to be coated with a dispersant, and showing no signs of agglomeration. After sintering (Supplementary Fig. 1b), noticeable changes in shape were observed, primarily attributed to two factors: 1) the formation of fibrous structures due to the sintering of PTFE particles, and 2) the removal of dispersant by thermal decomposition of the dispersant resulting. In the case of C1P99 and C5P95 having low MWCNT content, MWCNTs was rarely observed, but fibrous PTFE structures were visible on the surface, indicating the crystallization of PTFE during the sintering process [1, 2]. Starting from C10P90, buried MWCNTs within the sintered PTFE (relatively black and smooth areas) were observed. As PTFE content decreases, the area consisting only of MWCNTs increases, as seen in C100P0. The uniform dispersion of PTFE and the hierarchical nano-micro structure of the composite film surface can be crucial factors in achieving a desirable superhydrophobic level [3].

Electrical conductivity measurement was conducted for the same composition ratios (Supplementary Fig. 2). The electrical conductivity of MWCNT/PTFE nanocomposite film increased with MWCNT content, ranging from 0.92 to 44.96 S/cm (Supplementary Table 1). Similar to typical MWCNT/polymer composites [4, 5], the electrical conductivity of MWCNT/PTFE nanocomposite showed a rapid increase with low MWCNT content but tended to plateau at higher contents. In this study, there was a rapid increase in electrical conductivity up to C50P50 composition (36.98 S/cm), reaching a level similar to that of MWCNT film

(C100P0). However, additional increases in MWCNT content did not result in significant enhancement in electrical conductivity. Consequently, C50P50 condition was chosen as the optimal composition as GDL substrate.

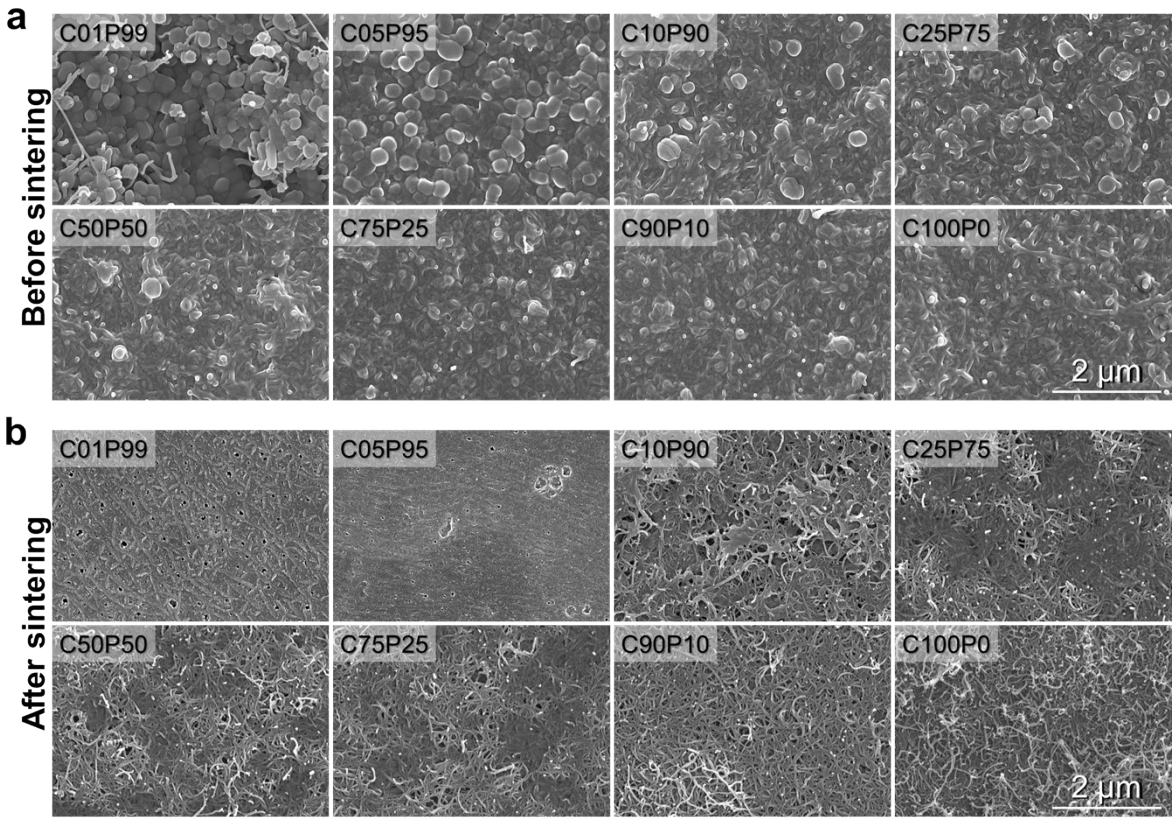

Figure S1 SEM images of MWCNT/PTFE nanocomposite films depending on MWCNT content (a**)** before and (b) after hot press sintering.

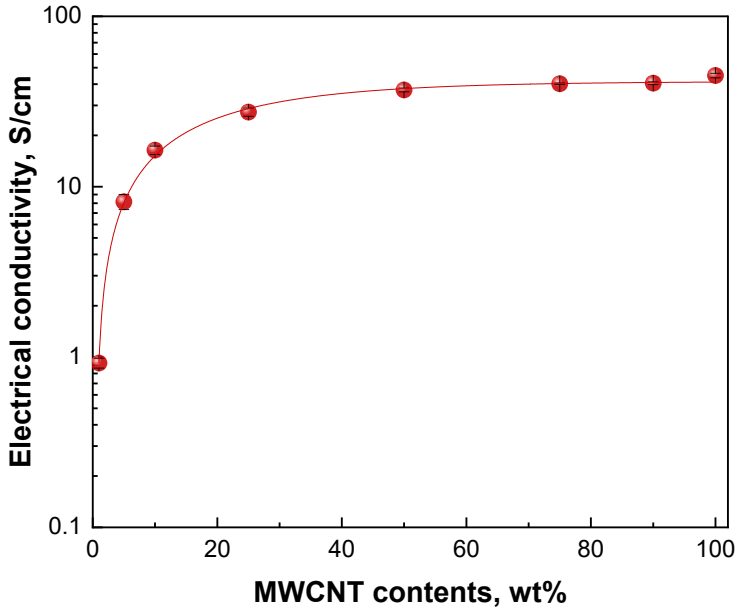

Figure S2. Electrical conductivity of MWCNT/PTFE nanocomposite films depending on MWCNT contents.

Table S1 Electrical conductivity of MWCNT/PTFE nanocomposite films depending on MWCNT contents.

Sample	MWCNT content, wt%	Resistance, Ω	Thickness, μm	Conductivity, S/cm
C01P99	1	63.33 ± 6.60	173.33 ± 14.82	0.92 ± 0.06
C05P95	5	6.23 ± 0.43	198.33 ± 6.24	8.16 ± 0.83
C10P90	10	6.03 ± 0.36	101.60 ± 3.01	16.39 ± 0.93
C25P75	25	2.83 ± 0.19	129.20 ± 2.48	27.42 ± 1.51
C50P50	50	1.82 ± 0.07	148.60 ± 2.58	36.98 ± 0.91
C75P25	75	1.63 ± 0.03	152.50 ± 3.20	40.19 ± 0.38
C90P10	90	3.24 ± 0.15	76.20 ± 2.32	40.53 ± 0.76
C100P0	100	2.00 ± 0.08	111.20 ± 3.76	44.96 ± 1.37

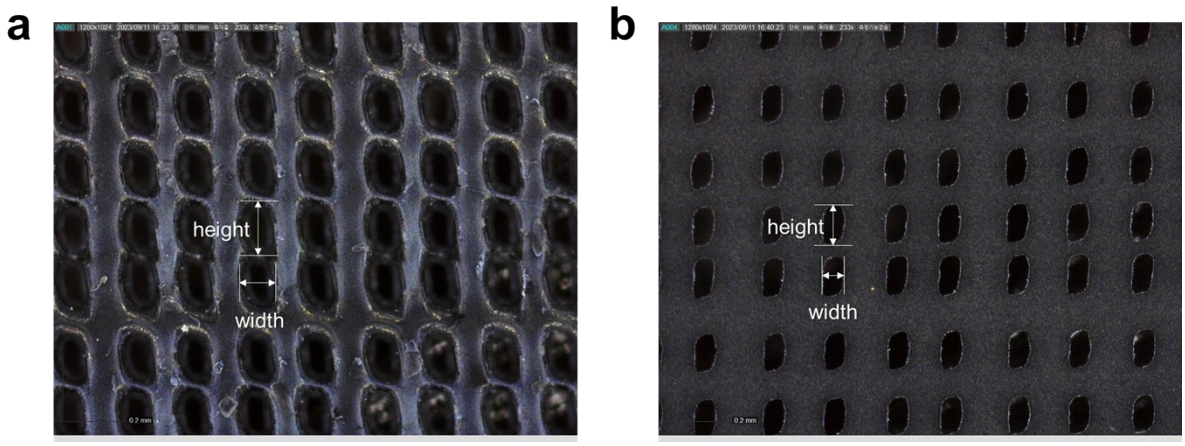

Figure S3 Microscope images of laser-perforated C50P50 nanocomposite film **a** front side and **b** back side.

Table S2 Hole size of laser-perforated C50P50 nanocomposite film.

	Upper hole, μm	Lower hole, μm
height	197.2 ± 7.1	115.9 ± 2.3
width	119.3 ± 3.9	65.7 ± 1.7

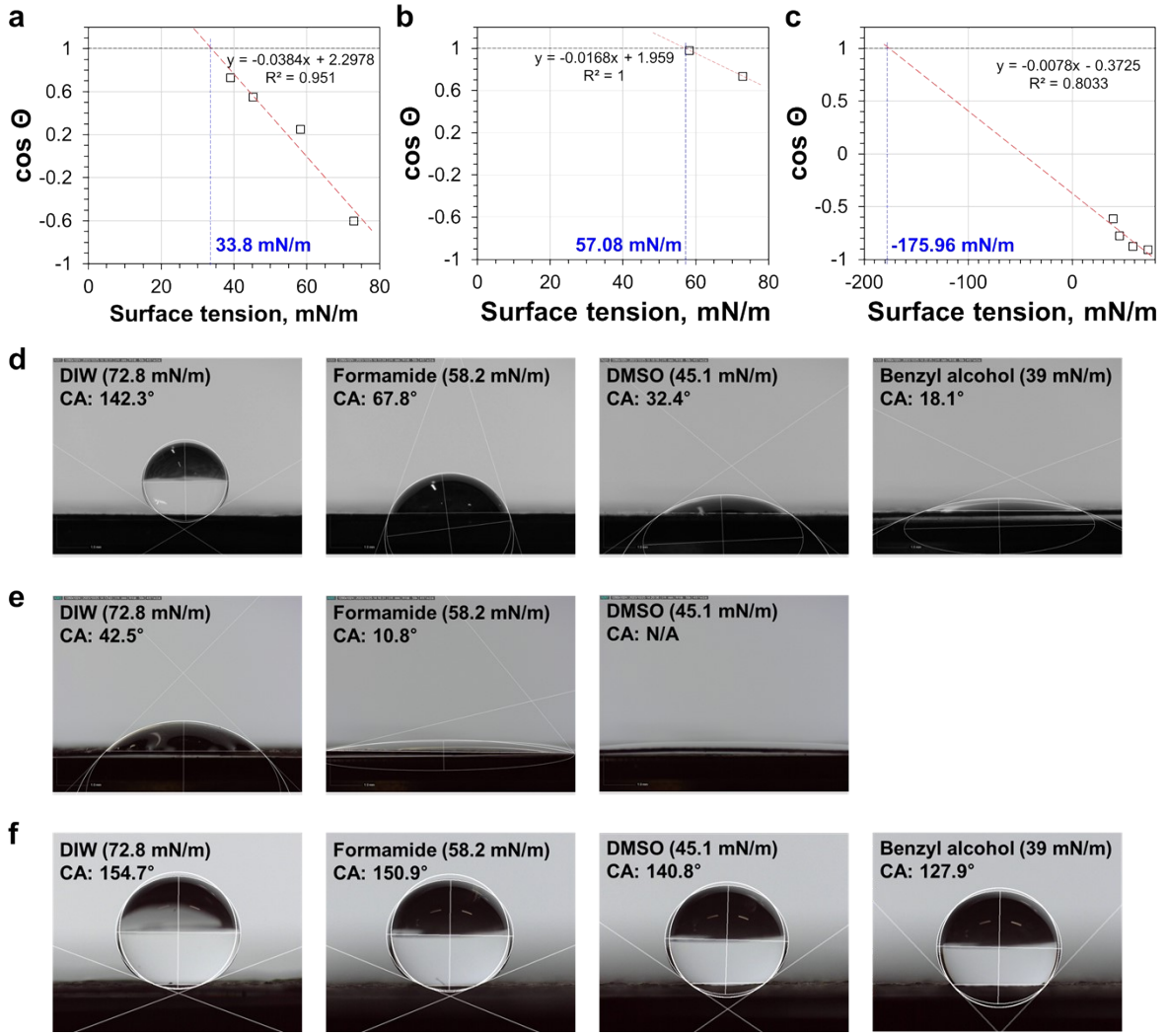

Figure S4 Zisman plot of (a) C50P50, (b) surface laser-treated C50P50 film, and (c) CB/PTFE MPL. Contact angles of (d) C50P50, (e) surface laser-treated C50P50 film, and (f) CB/PTFE MPL depending on different solvent.

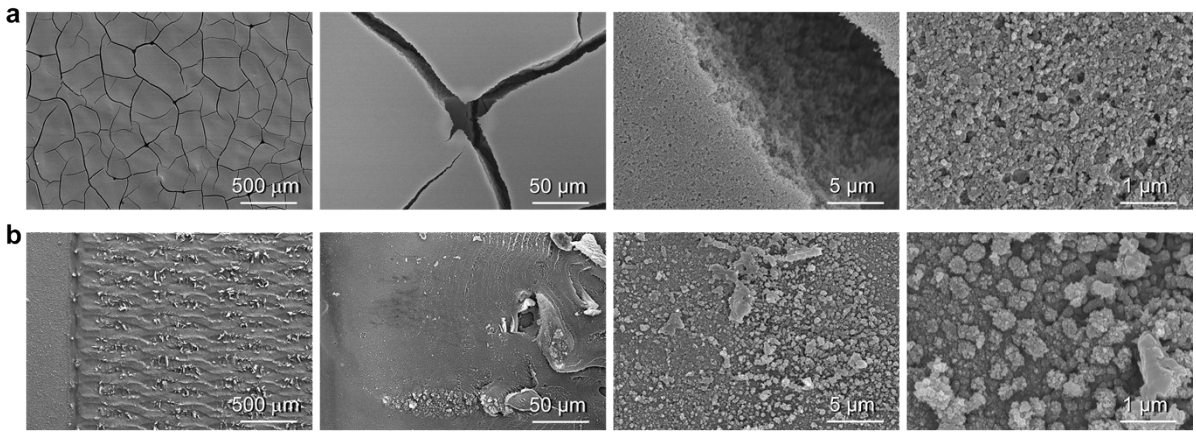

Figure S5 SEM images of (a) cGDL and (b) laser-induced surface of GDNL.

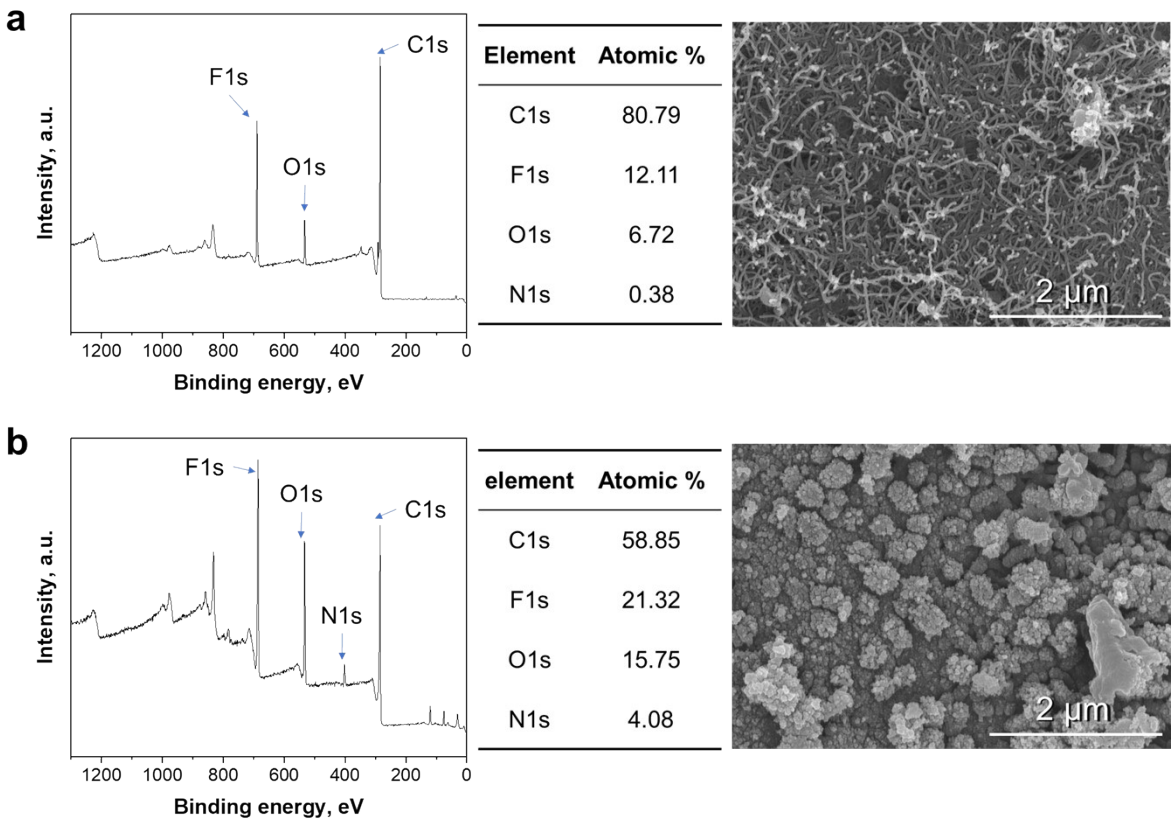

Figure S6 XPS results and SEM images of (a) C50P50 and (b) surface laser-treated C50P50 film.

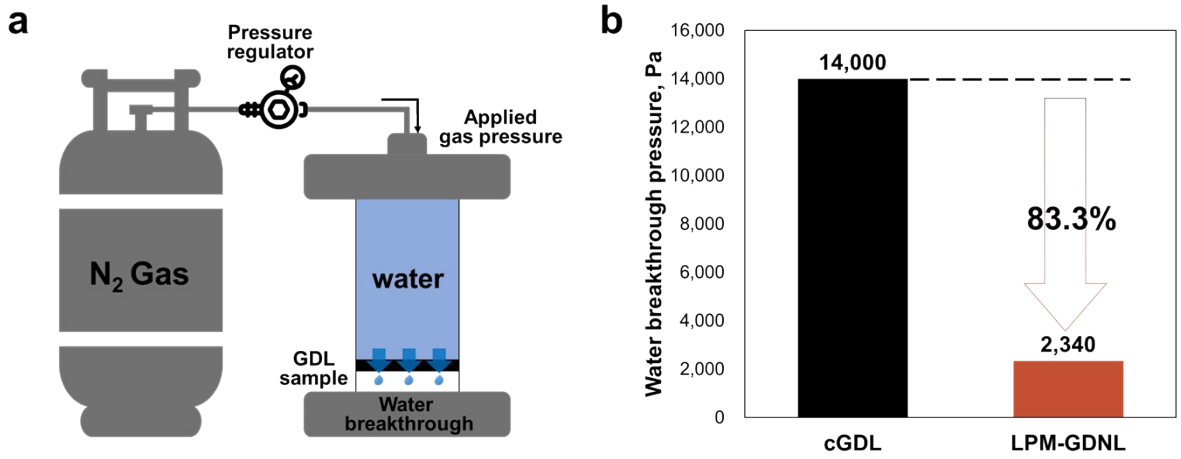

Figure S7. (a) Experimental set-up for water breakthrough pressure measurement and (b) water breakthrough pressure of cGDL and LPM-GDNL.

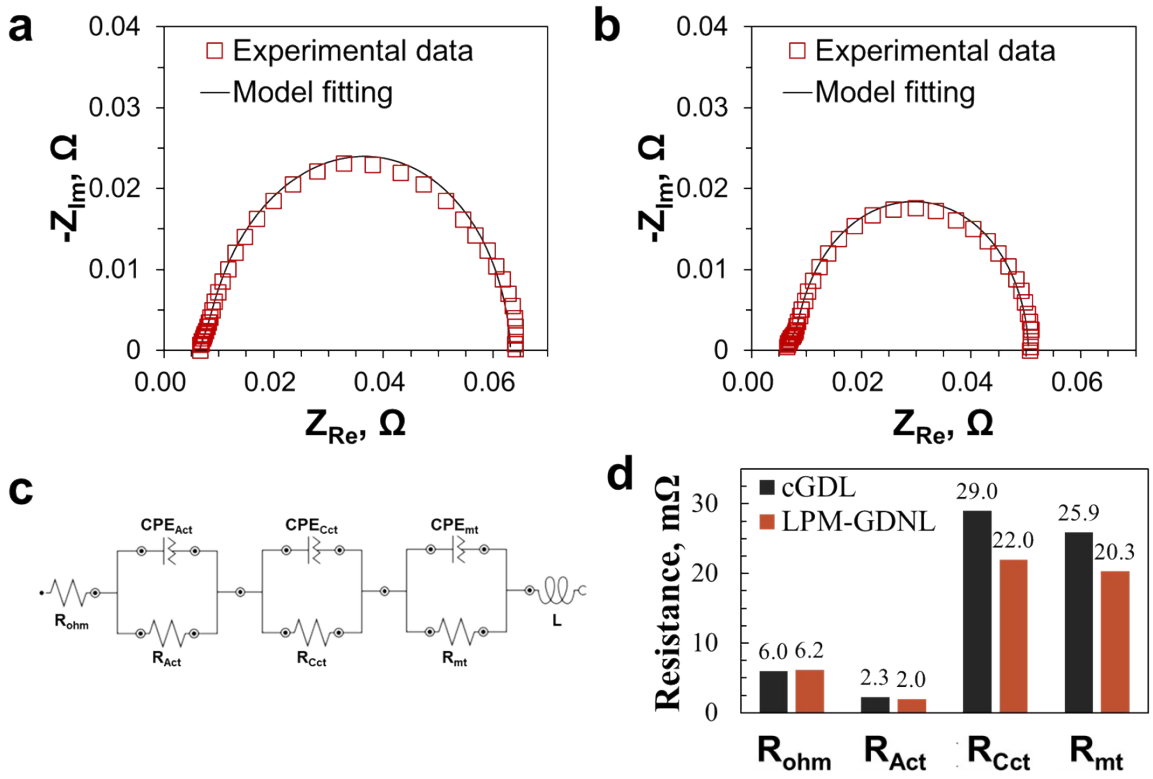

Figure S8. Electrochemical impedance spectroscope results for (b) cGDL and (c) LPM-GDNL of experimental data and model fitting. (c) Equivalent circuit model and (d) parameters.

Table S3. EIS equivalent circuit model parameters of cGDL and LPM-GDNL

	R_{ohm}, mΩ	R_{Act}, mΩ	R_{Cct}, mΩ	R_{mt}, mΩ
cGDL	6.0	2.3	29.0	25.9
LPM-GDNL	6.2	2.0	22	20.3

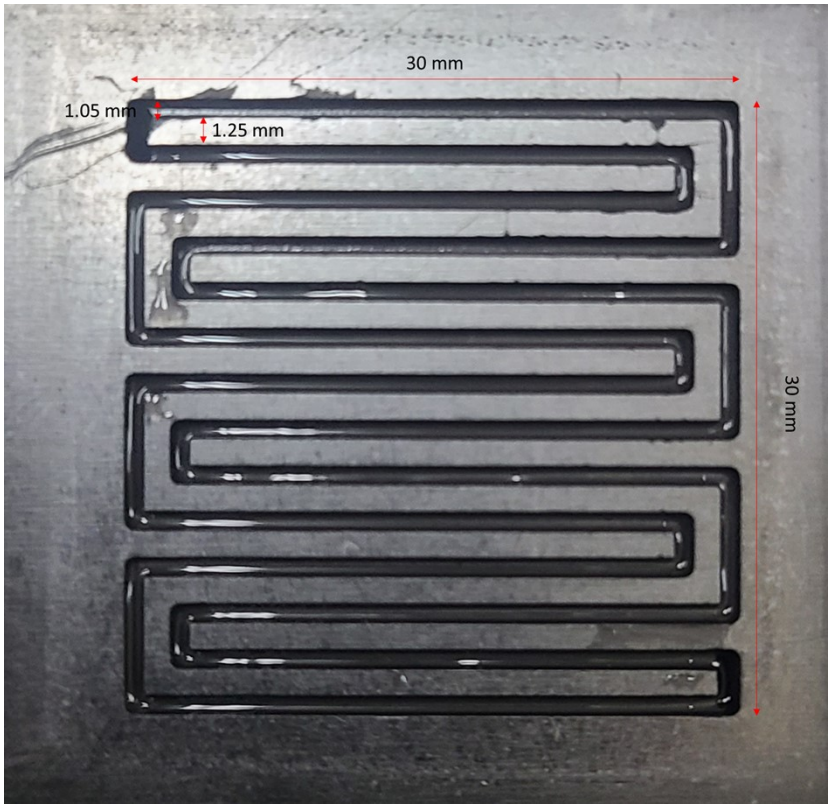

Figure S9. Serpentine flow field design of the bipolar plate.

References

1. Z. Z. Luo, Z. Z. Zhang, W. J. Wang, W. M. Liu and Q. J. Xue, *Materials Chemistry and Physics*, 2010, **119**, 40-47.
2. S. A. Khatipov, S. A. Serov, N. V. Sadovskaya and E. M. Konova, *Radiation Physics and Chemistry*, 2012, **81**, 256-263.
3. X. T. Chang, M. Y. Li, S. K. Tang, L. Shi, X. Q. Chen, S. C. Niu, X. J. Zhu, D. S. Wang and S. B. Sun, *Surface & Coatings Technology*, 2022, **434**.
4. Y. K. Min, T. Eom, H. Kim, D. H. Kang and S. E. Lee, *Polymers*, 2023, **15**.
5. Y. Sohn, D. Kim, S. Lee, M. Yin, J. Y. Song, W. Hwang, S. Park, H. Kim, Y. Ko and I. Han, *Journal of Materials Chemistry A*, 2014, **2**, 11465-11471.